Available online at www.sciencedirect.com

ScienceDirect

journal homepage: www.elsevier.com/locate/he

Partially crystallized Ni–Fe oxyhydroxides promotes oxygen evolution

Tianmi Tang [a], *Shihui Jiao* [b], *Jingyi Han* [a], *Zhenlu Wang* [a,**], *Jingqi Guan* [a,*]

[a] *Institute of Physical Chemistry, College of Chemistry, Jilin University, 2519 Jiefang Road, Changchun 130021, China*
[b] *College of Chemistry, Jilin University, 2519 Jiefang Road, Changchun 130021, China*

HIGHLIGHTS

- Partially crystallized nickel-iron oxyhydroxides are synthesized by a facile sol-gel method.
- The overpotential of $NiFe_{0.5}(OH)_x$ is only 265 mV at 10 mA cm^{-2}.
- $NiFe_{0.5}(OH)_x$ exhibits a low OER energy barrier of 31.5 kJ mol^{-1}.
- Synergy between Ni and Fe sites promotes charge transfer for the OER.

GRAPHICAL ABSTRACT

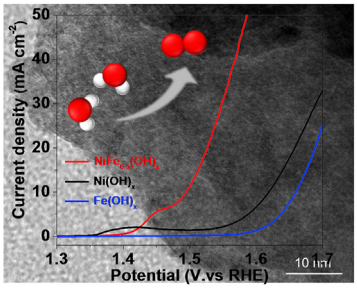

ARTICLE INFO

Article history:
Received 12 July 2022
Received in revised form
31 October 2022
Accepted 11 November 2022
Available online 5 December 2022

Keywords:
Nickel-iron
Oxygen evolution reaction
Partially crystallized hydroxide
Sol-gel method

ABSTRACT

The slow oxygen evolution reaction (OER) kinetics influences hydrogen production efficiency from water splitting. To break through the bottleneck of water splitting, it is urgent to develop efficient and economic electrocatalysts. Although NiFe-based catalysts exhibit outstanding OER activity, the complicated preparation process limits their large-scale synthesis and applications. Here, partially crystallized nickel-iron oxyhydroxides are synthesized by a facile sol-gel method. When the Fe/Ni mole ratio is 0.5:1, the $NiFe_{0.5}(OH)_x$ catalyst shows superior OER performance with a low OER overpotential of 265 mV and good durability. Kinetic studies show that the energy barrier of $NiFe_{0.5}(OH)_x$ is only 31.5 kJ mol^{-1}, much smaller than those of $Ni(OH)_x$ (41.0 kJ mol^{-1}) and $Fe(OH)_x$ (44.8 kJ mol^{-1}). The synergistic action between Ni and Fe sites not only facilitates mass and charge transfer, but also promotes the formation of *OOH intermediate for the OER.

* *Corresponding author.*
** *Corresponding author.*
E-mail addresses: wzl@jlu.edu.cn (Z. Wang), guanjq@jlu.edu.cn (J. Guan).
https://doi.org/10.1016/j.ijhydene.2022.11.118

Introduction

The increasing shortage of fossil energy and environmental problems force people to look for renewable and pollution-free energy. Hydrogen, as a clean and efficient energy that only generates water after burning, is expected to replace fossil fuels in the future [1–4]. As one of the most promising and effective H_2 production technologies, electrochemical water splitting has been widely concerned, which includes hydrogen evolution reaction (HER) and oxygen evolution reaction (OER). The productivity of electrochemical water splitting is limited by the OER because it is a slow four-proton coupled electron-transfer process [5–9]. At present, the best OER catalysts in industry are iridium oxide and ruthenium oxide, but the scarcity and high-cost restrain their wide commercial application [10,11]. To enhance the capacity of electrochemical water splitting, it is essential to design efficient and economical catalysts with abundant storage.

As substitutes for precious metal catalysts, transition metal materials are abundant on earth, which include transition metal oxides, hydroxides, nitrides, phosphates, sulfides and selenides [12–19]. In recent years, transition metal catalysts have made good progress in catalyzing OER, especially transition metal hydroxides, which have been widely studied due to their intrinsic catalytic activity. However, high overpotential is still needed to drive the OER. Nickel-based catalysts have high catalytic activity in theory, but they still cannot meet the commercial needs. By introducing other metal elements into nickel-based catalysts, the interaction between different metals can regulate the microenvironment of the active site and improve the performance of catalysts [20], for instance, Cr, Mn, Fe, Co, Cu, Mo and Ce have been introduced to enhance the OER performance [21–28].

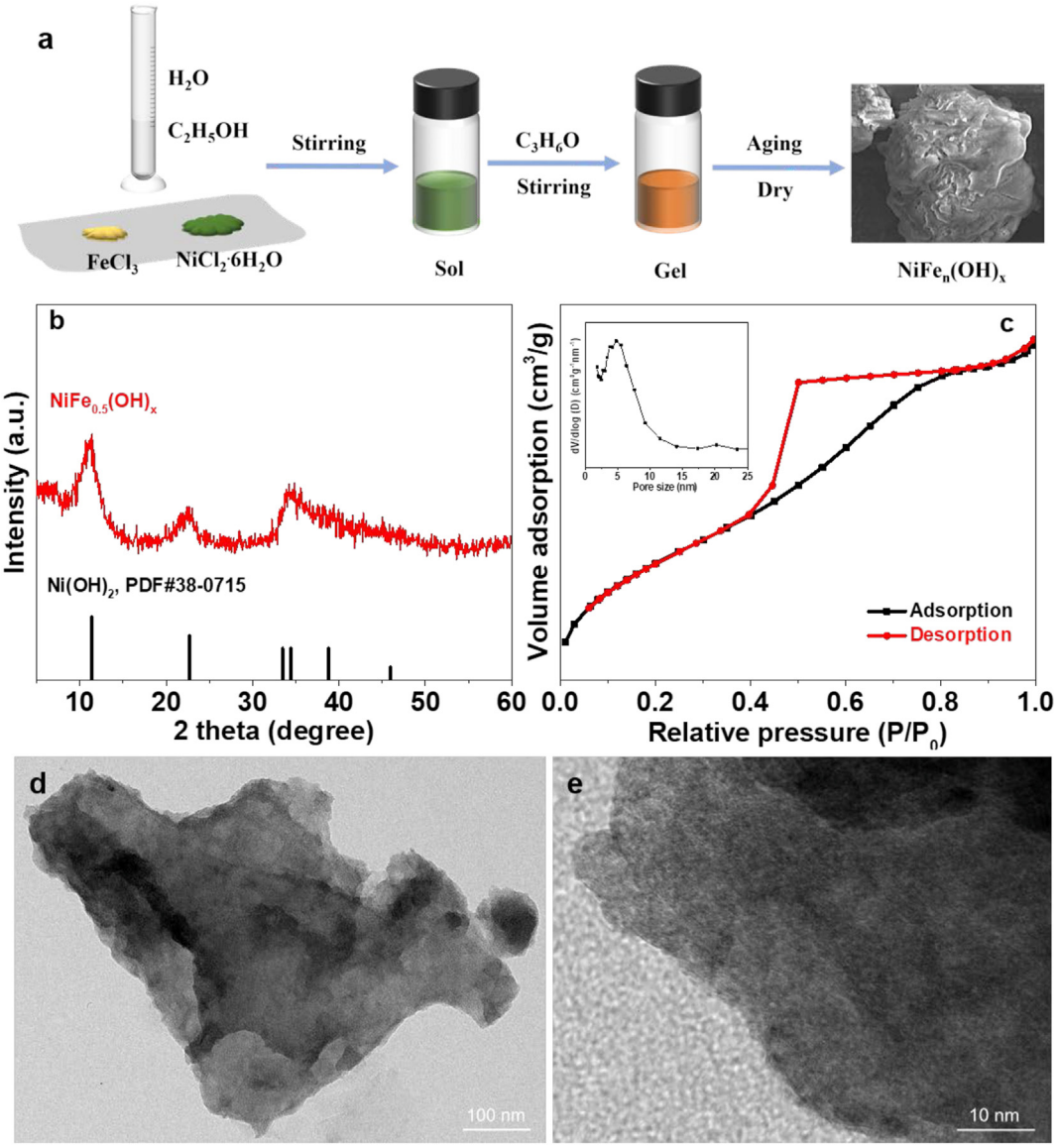

Fig. 1 – (a) Synthetic illustration of $NiFe_n(OH)_x$. (b) XRD patterns of $NiFe_{0.5}(OH)_x$. (c) N_2 adsorption–desorption isotherms of $NiFe_{0.5}(OH)_x$. Inset: pore-size distributions. TEM (d) and HRTEM image (e) of $NiFe_{0.5}(OH)_x$.

Introducing Fe into nickel based catalysts is a very effective regulation strategy. Theoretical calculations showed that Fe can induce electron transfer from Fe to Ni in Ni–Fe based catalysts [29,30]. In addition, Fe as a synergistic element not only induced the local directional transfer of electrons, but also increased the charge carrier density and conductivity of NiFe-hydroxyl oxides [31]. Zou et al. used DFT calculations to reveal that Fe can act as the active site in NiFe hydroxides for the OER [32]. Therefore, the development of NiFe-based catalysts is very promising.

Compared with single-metal nickel or iron catalysts, bimetallic nickel-iron hydroxides exhibit superior OER performance owing to the synergistic interaction between the two metals. Feng et al. synthesized Ni_2Fe-SDS-LDH/CFP catalyst by hydrothermal method, which demonstrated an overpotential (η_{10}) of 289 mV at 10 mA cm^{-2} for OER [33]. Lou et al. designed a self-template strategy to prepare Ni–Fe layered hydroxide hollow nanoprisms assembled by ultrathin nanosheets, which showed good OER activity (η_{10} = 280 mV) [34]. Studies have shown that the surface topography and amorphous structure of catalysts have a great influence on the OER activity, which can be improved by exposing more active sites [35]. Compared with crystalline solids, amorphous materials have disordered atomic combinations, metastable structures and a large number of defect structures [36]. Ding et al. synthesized amorphous Ni–Fe dihydroxide with oxygen vacancy using Cu_2O as the template, which showed an η_{10} of 310 mV [37]. However, the electrical resistance of amorphous oxyhydroxides is much higher than the corresponding crystalline oxides, resulting in larger charge transfer in the former, which is unfavorable at high current densities [38]. To enhance the charge transfer while maintain the catalytic activity, partial crystallization of amorphous oxyhydroxides is an efficient method.

NiFe oxyhydroxides were usually synthesized by hydrothermal method or template method, which are relatively complicated, leading to high production costs [39–42]. Here, we report a liable sol-gel method for the preparation of NiFe

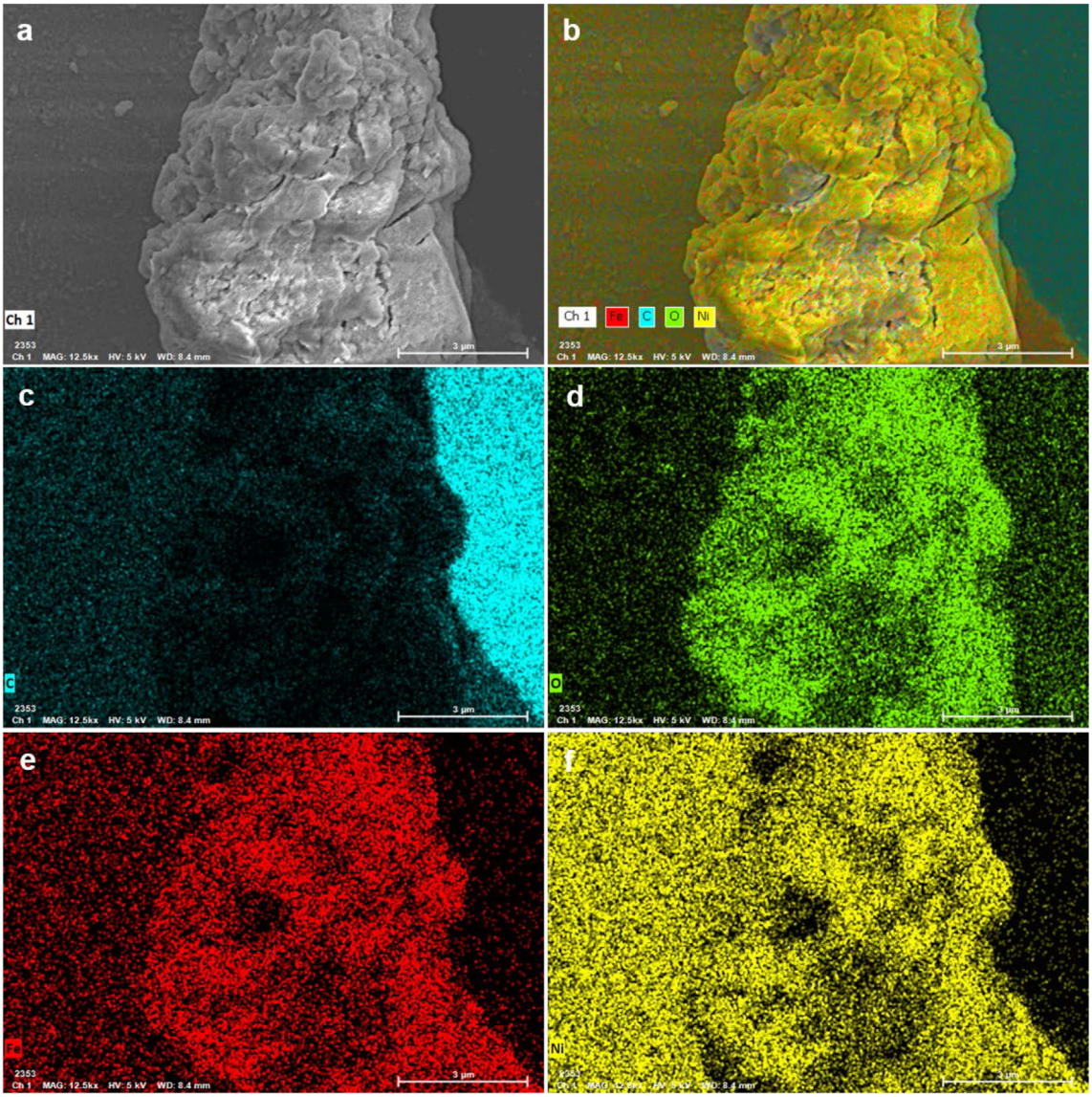

Fig. 2 – (a) SEM image of $NiFe_{0.5}(OH)_x$. (b–f) EDS mappings.

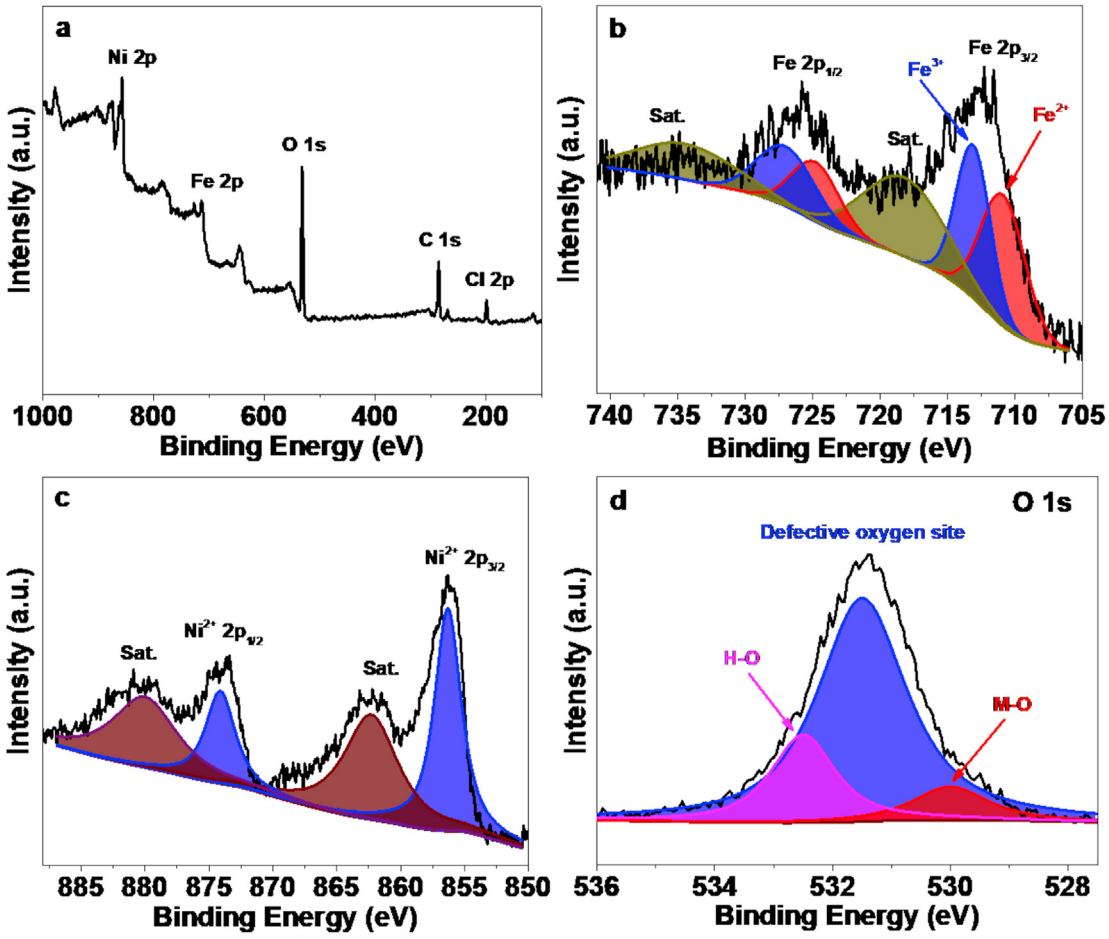

Fig. 3 – (a) XPS survey spectrum, and (b–d) XPS spectra of Fe 2p (b), Ni 2p (c), and O 1s (d) for the $NiFe_{0.5}(OH)_x$.

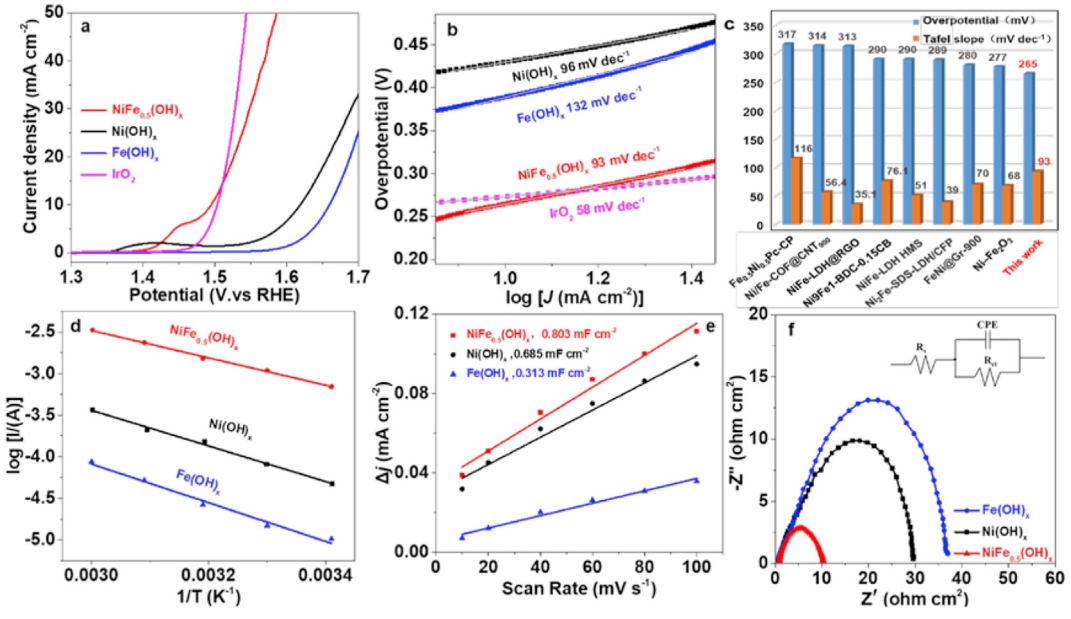

Fig. 4 – LSV curves (a) and Tafel slopes (b) in 1 M KOH. (c) Comparison of the performance of NiFe-based. (d) Arrhenius plots. (e) Capacitive Δj vs scan rate. (f) EIS plots in 1 M KOH.

Table 1 – OER performance on NiFe-based catalysts in 1.0 M KOH.

Catalyst	Overpotential (V vs. RHE)	Tafel slope	Ref.
$NiFe_{0.5}(OH)_x$	265	93	This work
Ni9Fe1-BDC-0.15CB	290	76.1	[52]
$Fe_{0.5}Ni_{0.5}$Pc-CP	317	116	[49]
Ni/Fe–COF@CNT-900	314	56.4	[50]
Ni–Fe_2O_3	277	68	[55]
FeNi@Gr-900	280	70	[54]
NiFe-LDH@RGO	313	35.1	[51]
Ni_2Fe-SDS-LDH/CFP	289	39	[33]
NiFe-LDH-HMS	290	51	[53]
Ni–Fe LDH	280	49.4	[34]
$Ni_3Fe_1O_x$@C-800	264	68	[48]
Ni_{32}Fe oxide	291	58	[56]
FN LDH/FNF-60	261	85.5	[57]
NiFe-LDH/CNT@GNR	261	78	[58]
FeNi LDH/MOF	272	34.1	[59]
Ni70Fe30(H)	292	30.4	[60]

oxyhydroxides with amorphous and partially crystallized structures. When Fe/Ni mole ratio is 0.5:1, the η_{10} of $NiFe_{0.5}(OH)_x$ is only 265 mV, lower than that on iridium oxide. According to the kinetic study, the energy barrier of $NiFe_{0.5}(OH)_x$ is 31.5 kJ mol^{-1}, significantly lower than that of $Ni(OH)_x$ (41 kJ mol^{-1}) and $Fe(OH)_x$ (44.8 kJ mol^{-1}) for the OER. Thus, the active site of $NiFe_{0.5}(OH)_x$ might to be Ni–O–Fe species.

Results and discussion

Gelatinous Ni–Fe oxyhydroxides ($NiFe_n(OH)_x$, n = 0.2, 0.4, 0.5, 0.6, 0.8) were prepared by a sol-gel strategy and dried at 40 °C as illustrated in Fig. 1a. The XRD pattern of $NiFe_{0.5}(OH)_x$ displays significant peaks around 11.2, 22.8, 34.4, 39.1, 46.4° (Fig. 1b), which are attributed to the bimetal NiFe oxyhydroxide, but these diffraction peaks are weak, indicating low crystallinity. Compared with $Ni(OH)_2$, these diffraction peaks are offset, demonstrating the fixation of Fe ions in the $Ni(OH)_2$ lattice. The BET specific surface area of $NiFe_{0.5}(OH)_x$ is 104.1 m^2 g^{-1}, and pore size is mainly concentrated at about 6 nm, suggesting that $NiFe_{0.5}(OH)_x$ is porous (Fig. 1c). From TEM image (Fig. 1d) and SEM image (Fig. S1), an irregular block structure for the $NiFe_{0.5}(OH)_x$ is typically observed. From HRTEM (Fig. 1e), some lattice fringes can be observed, again proving that the synthesized gelatinous $NiFe_{0.5}(OH)_x$ is partially crystallized. From the element mapping (Fig. 2), Ni and Fe elements were uniformly scattered in the $NiFe_{0.5}(OH)_x$.

XPS was employed to study the surface species and metal valence state of the synthesized $NiFe_{0.5}(OH)_x$ [43,44]. The presence of Ni, Fe, O and Cl elements can be clearly observed (Fig. 3a). The Fe 2p peak consists of four peaks: Fe $2p_{3/2}$ (713.6 eV), Fe $2p_{1/2}$ (724.7 eV) and two satellite peaks (Fig. 3b). The peaks at 710.9 and 713.1 eV are due to Fe^{2+} $2p_{3/2}$ and Fe^{3+} $2p_{3/2}$, respectively [45]. According to the peak area, the Fe^{3+}/Fe^{2+} molar ratio on the surface of the catalyst is about 1.3/1. In the Ni 2p spectrum of $NiFe_{0.5}(OH)_x$ (Fig. 3c), the two major peaks belong to the Ni^{2+} $2p_{3/2}$ (856.0 eV) and Ni^{2+} $2p_{1/2}$ (873.6 eV) orbits [46]. The O 1s XPS spectrum in Fig. 3d can be divided into lattice oxygen (Fe/Ni–O) (529.8 eV), defect oxygen (531.4 eV) and surface absorbed OH (532.5 eV) [47,48].

The OER electrocatalytic performance of $NiFe_{0.5}(OH)_x$, $Ni(OH)_x$, $Fe(OH)_x$ and IrO_2 is assessed in 1 M KOH. The $NiFe_{0.5}(OH)_x$ catalyst shows excellent OER catalytic performance, on which the initial overpotential is only 150 mV, and the η_{10} is as low as 265 mV, lower than $Ni(OH)_x$ (η_{10} = 389 mV), $Fe(OH)_x$ (η_{10} = 430 mV) and IrO_2 (η_{10} = 272 mV) (Fig. 4a). The impact of Fe/Ni molar ratio for OER performance was researched. The η_{10} first decreases and then increases with the increase of Fe/Ni mole ratio, and reaches the minimum value at Fe/Ni = 0.5:1 (Fig. S2a). The Tafel slope of $NiFe_{0.5}(OH)_x$ is 93 mV dec^{-1} (Fig. 4b, S2b), lower than $Ni(OH)_x$ (96 mV dec^{-1}) and $Fe(OH)_x$ (132 mV dec^{-1}), and also lower than those of $NiFe_n(OH)_x$ samples with other Fe/Ni mole ratios. The above results show that mono-metal Fe or Ni catalysts have worse OER performance than NiFe-based catalysts, indicating that the interaction between Fe and Ni significantly affects the catalytic activity. Fig. 4c and Table 1 show the overpotential and Tafel slopes of NiFe-based catalysts, showing that the η_{10} over the $NiFe_{0.5}(OH)_x$ is smaller than those over most catalysts, e.g. $Fe_{0.5}Ni_{0.5}$Pc-CP (317 mV) [49], Ni/Fe–COF@CNT 900 (314 mV) [50], NiFe-LDH@RGO (313 mV) [51], Ni9Fe1-BDC-0.15CB (290 mV) [52],

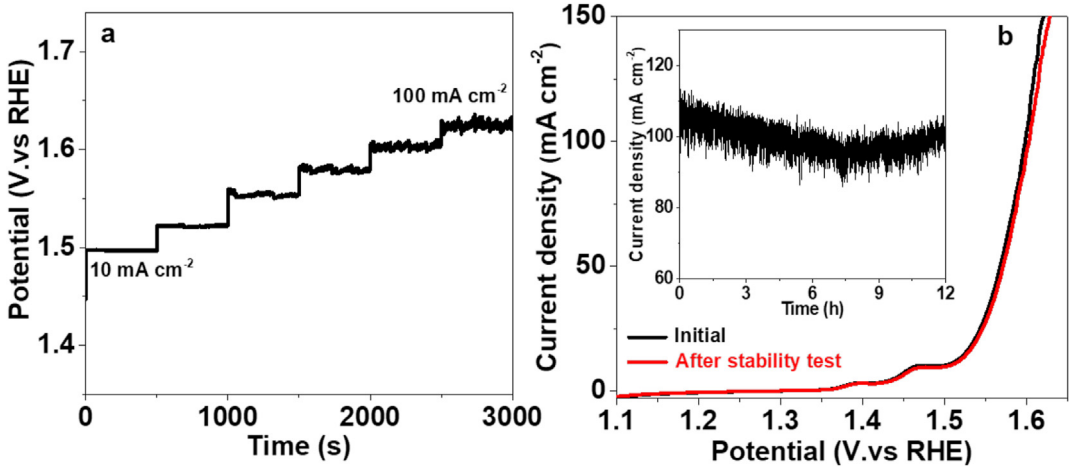

Fig. 5 – (a) Multi-current curves of $NiFe_{0.5}(OH)_x$ in 1 M KOH. (b) LSV curves of the fresh and used $NiFe_{0.5}(OH)_x$ (Inset: Chronoamperometric curve) in 1 M KOH.

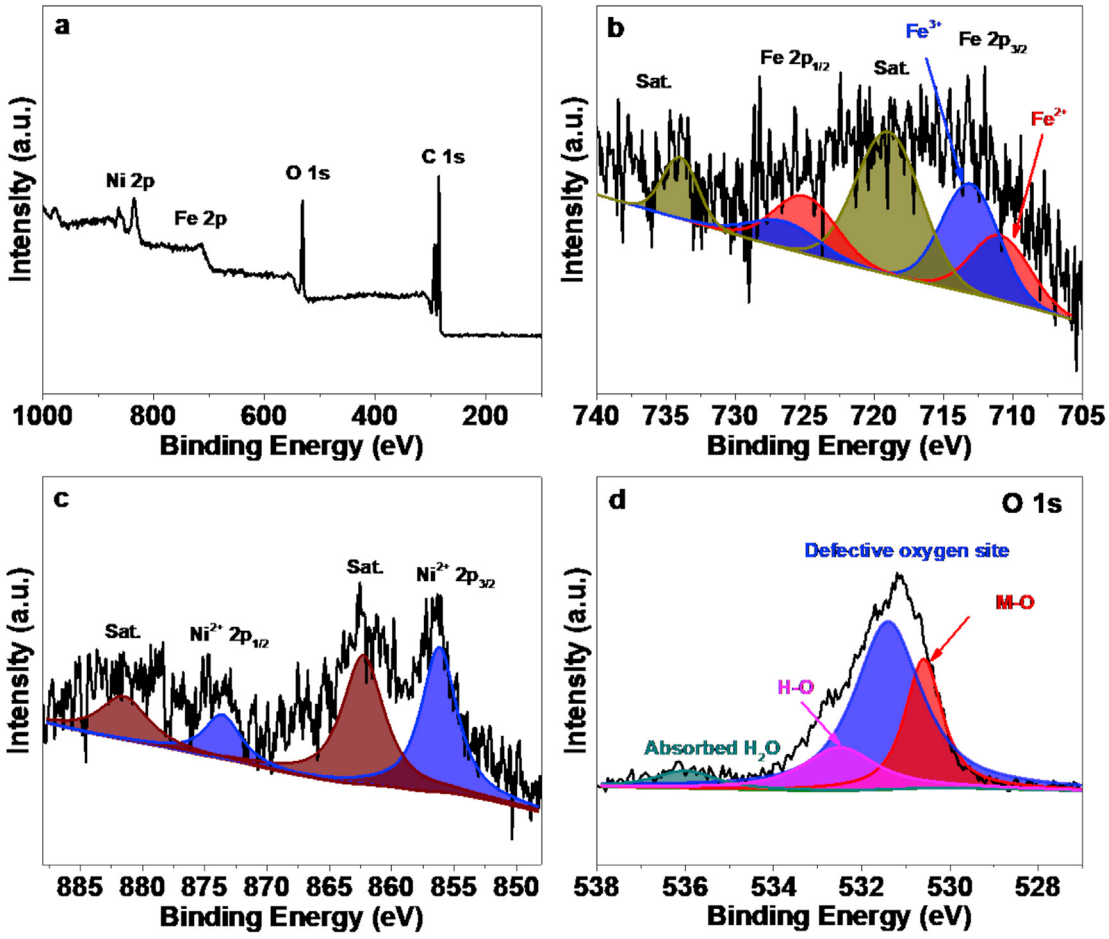

Fig. 6 – (a) XPS survey spectrum, and (b–d) XPS spectra of Fe 2p (b), Ni 2p (c), and O 1s (d) of the $NiFe_{0.5}(OH)_x$ after the OER.

NiFe-LDH-HMS (290 mV) [53], Ni_2Fe-SDS-LDH/CFP (289 mV) [33], FeNi@Gr-900 (280 mV) [54], and Ni–Fe_2O_3 nanoclews (277 mV) [55]. It proves that our synthesis method for Ni–Fe oxyhydroxides is very efficient.

Fig. S3 shows the redox peaks of $NiFe_{0.5}(OH)_x$, $Ni(OH)_x$ and $Fe(OH)_x$ catalysts. $Ni(OH)_x$ and $Fe(OH)_x$ have weak redox peaks, while $NiFe_{0.5}(OH)_x$ has a strong redox peak owing to the synergistic mechanism between Ni and Fe during OER. To study the kinetic energy barrier of the catalysts, we study the electrocatalytic activity at different temperatures (Fig. S4). With the increase of temperature, the OER activity increases, indicating that temperature is related to chemical rate constant. According to the Arrhenius formula: $\left.\frac{\partial(\log i_k)}{\partial\left(\frac{1}{T}\right)}\right|_h = \frac{\Delta H^*}{2.303R}$, i_k is the dynamic current when the overpotential is 300 mV, T is Kelvin temperature, and R is 8.314 J/(mol·K) [61,62]. The kinetic barrier of $NiFe_{0.5}(OH)_x$ is computed to be 31.5 kJ mol^{-1}, lower than that of $Ni(OH)_x$ (41.0 kJ mol^{-1}) and $Fe(OH)_x$ (44.8 kJ mol^{-1}) (Fig. 4d). It can be inferred that the introduction of Fe ions to the Ni-based oxyhydroxide effectively regulates the local electronic structure around active Ni sites, and the formation of hydroxyl group enhances the adsorption capacity of the intermediates in the OER process. The most active structure in OER process is the structure in which Fe and Ni are in close contact [63].

The effective active site of electrocatalytic reaction can be evaluated by ECSA and C_{dl}, as displayed in Fig. 4e and Figs. S5–S7. $NiFe_{0.5}(OH)_x$ shows higher C_{dl} (0.803 mF cm^{-2}) than $Ni(OH)_x$ and $Fe(OH)_x$, indicating good synergistic effect between Ni and Fe in the $NiFe_{0.5}(OH)_x$. The ECSA of $NiFe_{0.5}(OH)_x$ is 20 cm^2, that is bigger than the single metal $Ni(OH)_x$ (17 cm^2) and $Fe(OH)_x$ (8 cm^2), indicating that $NiFe_{0.5}(OH)_x$ possesses more OER active sites. In addition, the specific activity of $NiFe_{0.5}(OH)_x$ is far larger than $Ni(OH)_x$ and $Fe(OH)_x$ (Fig. S8) [64]. The charge transfer capability can be evaluated by charge transfer resistance (R_{ct}) [65]. According to the Nyquist plots (Fig. 4f), the R_{ct} values of $NiFe_{0.5}(OH)_x$, $Ni(OH)_x$ and $Fe(OH)_x$ are 10, 30 and 37 Ω cm^{-2}, respectively, indicating that the $NiFe_{0.5}(OH)_x$ catalyst is more favorable for charge transfer in the OER process. In addition, by comparing R_{ct} with different Fe/Ni molar ratios (Fig. S9), the R_{ct} value of $NiFe_{0.5}(OH)_x$ was the smallest. When the overpotential is 350 mV, the turnover frequency (TOF_{Ni+Fe}) of $NiFe_{0.5}(OH)_x$ is 0.027 s^{-1}, far larger than $Ni(OH)_x$ (0.0029 s^{-1}) and $Fe(OH)_x$ (0.00044 s^{-1}), indicating that the $NiFe_{0.5}(OH)_x$ catalyst has higher intrinsic activity (Fig. S10) [66,67].

The stability is an important indicator for evaluating catalytic performance. The stability of $NiFe_{0.5}(OH)_x$ is evaluated by multi-step chronopotentiometric measurement (Fig. 5a). The potential can reach a stable state immediately at different

current densities. The stability of $NiFe_{0.5}(OH)_x$ is further evaluated at 100 mA cm^{-2}, demonstrating that the catalytic activity can be held for more than 12 h without significant change in the catalytic activity after chronoamperometric measurement (Fig. 5b). These results indicate that $NiFe_{0.5}(OH)_x$ has good mass transfer ability and outstanding durability.

XPS was performed to reveal the composition and metal valence states on the surface of $NiFe_{0.5}(OH)_x$ catalyst after OER stability test (Fig. 6). Ni and Fe elements are detected on the catalyst surface. Partial Fe^{2+} ions on the surface were oxidized to Fe^{3+}, and the relative content of Fe^{3+}/Fe^{2+} increased to 1.4/1, suggesting that Fe^{3+} in high valence state plays a key role in OER process. In addition, the change of relative content of oxygen species after OER test is compared to that before OER test, indicating that surface oxygen species are involved in the reaction. Fig. S11 shows the XRD patterns of $NiFe_{0.5}(OH)_x$ after the stability test. The results show that the peak of $NiFe_{0.5}(OH)_x$ after OER is weaker than fresh $NiFe_{0.5}(OH)_x$ due to a mass of water molecules adsorbed on the catalyst surface [68].

Conclusions

We developed a simple sol-gel method to prepare partially crystallized nickel-iron oxyhydroxides with good OER catalytic activity, The η_{10} on $NiFe_{0.5}(OH)_x$ is only 265 mV, which is much lower than most NiFe-based catalysts reported previously. The kinetic studies showed that Ni–Fe oxyhydroxides have lower OER barrier than single-metal Fe/Ni hydroxyl oxides, demonstrating that the interaction between Ni and Fe accelerates electron transfer and promotes water oxidation.

Declaration of competing interest

The authors declare that they have no known competing financial interests or personal relationships that could have appeared to influence the work reported in this paper.

Acknowledgments

This work was supported by the Education Department of Jilin Province (No. JJKH20220967KJ, No. JJKH20220968CY), the National Natural Science Foundation of China (No. 22075099), the Natural Science Foundation of Jilin Province (No. 20220101051JC).

Appendix A. Supplementary data

Supplementary data to this article can be found online at https://doi.org/10.1016/j.ijhydene.2022.11.118.

REFERENCES

[1] Zhang K, Zou R. Advanced transition metal-based OER electrocatalysts: current status, opportunities, and challenges. Small 2021;17:2100129.
[2] Bai X, Guan J. MXenes for electrocatalysis applications: modification and hybridization. Chin J Catal 2022;43:2057–90.
[3] Tang T, Wang Z, Guan J. A review of defect engineering in two-dimensional materials for electrocatalytic hydrogen evolution reaction. Chin J Catal 2022;43:636–78.
[4] Anantharaj S, Noda S, Jothi VR, Yi S, Driess M, Menezes PW. Strategies and perspectives to catch the missing pieces in energy-efficient hydrogen evolution reaction in alkaline media. Angew Chem Int Ed 2021;60:18981–9006.
[5] Talib SH, Lu Z, Yu X, Ahmad K, Bashir B, Yang Z, et al. Theoretical inspection of M1/PMA single-atom electrocatalyst: ultra-high performance for water splitting (HER/OER) and oxygen reduction reactions (OER). ACS Catal 2021;11:8929–41.
[6] Gu J, Magagula S, Zhao J, Chen Z. Boosting ORR/OER activity of graphdiyne by simple heteroatom doping. Small Methods 2019;3:1800550.
[7] Huang R, Wen Y, Peng H, Zhang B. Improved kinetics of OER on Ru-Pb binary electrocatalyst by decoupling proton-electron transfer. Chin J Catal 2022;43:130–8.
[8] Guan J, Bai X, Tang T. Recent progress and prospect of carbon-free single-site catalysts for the hydrogen and oxygen evolution reactions. Nano Res 2022;15:818–37.
[9] Anantharaj S, Aravindan V. Developments and perspectives in 3d transition-metal-based electrocatalysts for neutral and near-neutral water electrolysis. Adv Energy Mater 2020;10:1902666.
[10] Anantharaj S, Noda S. Amorphous catalysts and electrochemical water splitting: an untold story of harmony. Small 2020;16:1905779.
[11] Bai X, Wang L, Nan B, Tang T, Niu X, Guan J. Atomic manganese coordinated to nitrogen and sulfur for oxygen evolution. Nano Res 2022;15:6019–25.
[12] Song F, Bai L, Moysiadou A, Lee S, Hu C, Liardet L, et al. Transition metal oxides as electrocatalysts for the oxygen evolution reaction in alkaline solutions: an application-inspired renaissance. J Am Chem Soc 2018;140:7748–59.
[13] Che Q, Li Q, Chen X, Tan Y, Xu X. Assembling amorphous (Fe-Ni)Co_x-OH/Ni_3S_2 nanohybrids with S-vacancy and interfacial effects as an ultra-highly efficient electrocatalyst: inner investigation of mechanism for alkaline water-to-hydrogen/oxygen conversion. Appl Catal, B 2020;263:118338.
[14] Wang Z, Xu L, Huang F, Qu L, Li J, Owusu KA, et al. Copper–nickel nitride nanosheets as efficient bifunctional catalysts for hydrazine-assisted electrolytic hydrogen production. Adv Energy Mater 2019;9:1900390.
[15] Kong F, Zhang W, Sun L, Huo L, Zhao H. Interface electronic coupling in hierarchical FeLDH(FeCo)/$Co(OH)_2$ arrays for efficient electrocatalytic oxygen evolution. ChemSusChem 2019;12:3592–601.
[16] Anantharaj S, Noda S, Driess M, Menezes PW. The pitfalls of using potentiodynamic polarization curves for Tafel analysis in electrocatalytic water splitting. ACS Energy Lett 2021;6:1607–11.
[17] Anantharaj S, Noda S. How properly are we interpreting the Tafel lines in energy conversion electrocatalysis? Mater Today Energy 2022;29:101123.
[18] Anantharaj S, Noda S. iR drop correction in electrocatalysis: everything one needs to know. J Mater Chem 2022;10:9348–54.
[19] Tang T, Wang Z, Guan J. Electronic structure regulation of single-site M-N-C electrocatalysts for carbon dioxide reduction. Acta Phys - Chim Sin 2023;39:2208033.
[20] Shin C-H, Wei Y, Park G, Kang J, Yu J-S. High performance binder-free Fe–Ni hydroxides on nickel foam prepared in piranha solution for the oxygen evolution reaction. Sustain Energ Fuels 2020;4:6311–20.

[21] Chen S, Yu C, Cao Z, Huang X, Wang S, Zhong H. Trimetallic NiFeCr-LDH/MoS_2composites as novel electrocatalyst for OER. Int J Hydrogen Energy 2021;46:7037–46.
[22] Morales DM, Kazakova MA, Dieckhöfer S, Selyutin AG, Golubtsov GV, Schuhmann W, et al. Trimetallic Mn-Fe-Ni oxide nanoparticles supported on multi-walled carbon nanotubes as high-performance bifunctional ORR/OER electrocatalyst in alkaline media. Adv Funct Mater 2020;30:1905992.
[23] Gopi S, Vadivel S, Pinto LMC, Syed A, Kathiresan M, Yun K. Non-noble metal (Ni, Cu)-carbon composite derived from porous organic polymers for high-performance seawater electrolysis. Environ Pollut 2021;289:117861.
[24] Zai SF, Gao XY, Yang CC, Jiang Q. Ce-modified $Ni(OH)_2$ nanoflowers supported on $NiSe_2$ octahedra nanoparticles as high-efficient oxygen evolution electrocatalyst. Adv Energy Mater 2021;11:2101266.
[25] Han J, Zhang M, Bai X, Duan Z, Tang T, Guan J. Mesoporous Mn–Fe oxyhydroxides for oxygen evolution. Inorg Chem Front 2022;9:3559–65.
[26] Bai X, Duan Z, Nan B, Wang L, Tang T, Guan J. Unveiling the active sites of ultrathin Co-Fe layered double hydroxides for the oxygen evolution reaction. Chin J Catal 2022;43:2240–8.
[27] Anantharaj S, Kundu S, Noda S. Worrisome exaggeration of activity of electrocatalysts destined for steady-state water electrolysis by polarization curves from transient techniques. J Electrochem Soc 2022;169:014508.
[28] Anantharaj S, Kundu S, Noda S. "The Fe Effect": a review unveiling the critical roles of Fe in enhancing OER activity of Ni and Co based catalysts. Nano Energy 2021;80:105514.
[29] Conesa JC. Electronic structure of the (undoped and Fe-doped) NiOOH O_2 evolution electrocatalyst. J Phys Chem C 2016;120:18999–9010.
[30] Görlin M, Chernev P, Paciok P, Tai C-W, Ferreira de Araújo J, Reier T, et al. Formation of unexpectedly active Ni–Fe oxygen evolution electrocatalysts by physically mixing Ni and Fe oxyhydroxides. Chem Commun 2019;55:818–21.
[31] Trotochaud L, Young SL, Ranney JK, Boettcher SW. Nickel–iron oxyhydroxide oxygen-evolution electrocatalysts: the role of intentional and incidental iron incorporation. J Am Chem Soc 2014;136:6744–53.
[32] Zou S, Burke MS, Kast MG, Fan J, Danilovic N, Boettcher SW. Fe (Oxy)hydroxide oxygen evolution reaction electrocatalysis: intrinsic activity and the roles of electrical conductivity, substrate, and dissolution. Chem Mater 2015;27:8011–20.
[33] Zhong H, Cheng X, Xu H, Li L, Li D, Tang P, et al. Carbon fiber paper supported interlayer space enlarged Ni_2Fe-LDHs improved OER electrocatalytic activity. Electrochim Acta 2017;258:554–60.
[34] Yu L, Yang JF, Guan BY, Lu Y, Lou XW. Hierarchical hollow nanoprisms based on ultrathin Ni-Fe layered double hydroxide nanosheets with enhanced electrocatalytic activity towards oxygen evolution. Angew Chem Int Ed 2018;57:172–6.
[35] Lu X, Zhao C. Electrodeposition of hierarchically structured three-dimensional nickel–iron electrodes for efficient oxygen evolution at high current densities. Nat Commun 2015;6:6616.
[36] Kanan Matthew W, Nocera Daniel G. In situ formation of an oxygen-evolving catalyst in neutral water containing phosphate and Co^{2+}. Science 2008;321:1072–5.
[37] Tian T, Zheng M, Lin J, Meng X, Ding Y. Amorphous Ni–Fe double hydroxide hollow nanocubes enriched with oxygen vacancies as efficient electrocatalytic water oxidation catalysts. Chem Commun 2019;55:1044–7.
[38] Bai X, Fan Y, Hou C, Tang T, Guan J. Partial crystallization of Co–Fe oxyhydroxides towards enhanced oxygen evolution activity. Int J Hydrogen Energy 2022;47:16711–8.
[39] Acharya P, Manso RH, Hoffman AS, Bakovic SIP, Kékedy-Nagy L, Bare SR, et al. Fe coordination environment, Fe-incorporated $Ni(OH)_2$ phase, and metallic core are key structural components to active and stable nanoparticle catalysts for the oxygen evolution reaction. ACS Catal 2022;12:1992–2008.
[40] Wang Y, Li Y, Ding L, Chen Z, Ong A, Lu W, et al. NiFe (sulfur) oxyhydroxide porous nanoclusters/Ni foam composite electrode drives a large-current-density oxygen evolution reaction with an ultra-low overpotential. J Mater Chem 2019;7:18816–22.
[41] Wang Z, Wang Y, Zhang N, Ma L, Sun J, Yu C, et al. Highly efficient oxygen evolution catalysis achieved by NiFe oxyhydroxide clusters anchored on carbon black. J Mater Chem A 2022;10:10342–9.
[42] Görlin M, Ferreira de Araújo J, Schmies H, Bernsmeier D, Dresp S, Gliech M, et al. Tracking catalyst redox states and reaction dynamics in Ni–Fe oxyhydroxide oxygen evolution reaction electrocatalysts: the role of catalyst support and electrolyte pH. J Am Chem Soc 2017;139:2070–82.
[43] Anantharaj S, Sugime H, Chen B, Akagi N, Noda S. Boosting the oxygen evolution activity of copper foam containing trace Ni by intentionally supplementing Fe and forming nanowires in anodization. Electrochim Acta 2020;364:137170.
[44] Anantharaj S, Sugime H, Noda S. Chemical leaching of inactive Cr and subsequent electrochemical resurfacing of catalytically active sites in stainless steel for high-rate alkaline hydrogen evolution reaction. ACS Appl Energy Mater 2020;3:12596–606.
[45] Wei H-l, Tan A-d, Hu S-z, Piao J-h, Fu Z-y. Efficient spinel iron-cobalt oxide/nitrogen-doped ordered mesoporous carbon catalyst for rechargeable zinc-air batteries. Chin J Catal 2021;42:1451–8.
[46] Liu H, Jia Q, Huang S, Yang L, Wang S, Zheng L, et al. Ultra-small Ru nanoparticles embedded on Fe–$Ni(OH)_2$ nanosheets for efficient water splitting at a large current density with long-term stability of 680 hours. J Mater Chem A 2022;10:4817–24.
[47] Liu N, Guan J. Core–shell Co_3O_4@FeO_x catalysts for efficient oxygen evolution reaction. Mater Today Energy 2021;21:100715.
[48] Bai X, Ma Y, Wang Q, Guan J. Core-shell Ni_3Fe-based nanocomposites for the oxygen evolution reaction. Int J Hydrogen Energy 2022;47:2304–12.
[49] Qi D, Chen X, Liu W, Liu C, Liu W, Wang K, et al. A Ni/Fe-based heterometallic phthalocyanine conjugated polymer for the oxygen evolution reaction. Inorg Chem Front 2020;7:642–6.
[50] Xu Q, Qian J, Luo D, Liu G, Guo Y, Zeng G. Ni/Fe clusters and nanoparticles confined by covalent organic framework derived carbon as highly active catalysts toward oxygen reduction reaction and oxygen evolution reaction. Adv Sustainable Syst 2020;4:2000115.
[51] Tan L, Su Z, Yang R, Tao J, Zhao D, Zhang Z, et al. Oxygen evolution catalytic performance of quantum dot nickel-iron double hydroxide/reduced graphene oxide composites. Mater Lett 2018;231:24–7.
[52] Tan J, He X, Yin F, Chen B, Liang X, Li G, et al. Fe doped metal organic framework (Ni)/carbon black nanosheet as highly active electrocatalyst for oxygen evolution reaction. Int J Hydrogen Energy 2020;45:21431–41.
[53] Zhong H, Liu T, Zhang S, Li D, Tang P, Alonso-Vante N, et al. Template-free synthesis of three-dimensional NiFe-LDH hollow microsphere with enhanced OER performance in alkaline media. J Energy Chem 2019;33:130–7.
[54] Tu Y, Ren P, Deng D, Bao X. Structural and electronic optimization of graphene encapsulating binary metal for highly efficient water oxidation. Nano Energy 2018;52:494–500.

[55] Samanta A, Das S, Jana S. Doping of Ni in α-Fe_2O_3 nanoclews to boost oxygen evolution electrocatalysis. ACS Sustain Chem Eng 2019;7:12117–24.
[56] Yu M, Moon G, Bill E, Tüysüz H. Optimizing Ni–Fe oxide electrocatalysts for oxygen evolution reaction by using hard templating as a toolbox. ACS Appl Energy Mater 2019;2:1199–209.
[57] Zeng L, Yang L, Lu J, Jia J, Yu J, Deng Y, et al. One-step synthesis of Fe-Ni hydroxide nanosheets derived from bimetallic foam for efficient electrocatalytic oxygen evolution and overall water splitting. Chin Chem Lett 2018;29:1875–8.
[58] Yin X, Hua Y, Hao W, Yang J, Gao Z. Hierarchical nanocomposites of nickel/iron-layered double hydroxide ultrathin nanosheets strong-coupled with nanocarbon networks for enhanced oxygen evolution reaction. Electrochim Acta 2022;420:140455.
[59] Zheng F, Zhang W, Zhang X, Zhang Y, Chen W. Sub-2 nm ultrathin and robust 2D FeNi layered double hydroxide nanosheets packed with 1D FeNi-MOFs for enhanced oxygen evolution electrocatalysis. Adv Funct Mater 2021;31:2103318.
[60] Lee E, Park A-H, Park H-U, Kwon Y-U. Facile sonochemical synthesis of amorphous NiFe-(oxy)hydroxide nanoparticles as superior electrocatalysts for oxygen evolution reaction. Ultrason Sonochem 2018;40:552–7.
[61] Swierk JR, Klaus S, Trotochaud L, Bell AT, Tilley TD. Electrochemical study of the energetics of the oxygen evolution reaction at nickel iron (Oxy)Hydroxide catalysts. J Phys Chem C 2015;119:19022–9.
[62] Zhang B, Zheng X, Voznyy O, Comin R, Bajdich M, García-Melchor M, et al. Homogeneously dispersed multimetal oxygen-evolving catalysts. Science 2016;352:333–7.
[63] Xiang D, Bo X, Gao X, Zhang C, Du C, Zheng F, et al. Novel one-step synthesis of core@shell iron–nickel alloy nanoparticles coated by carbon layers for efficient oxygen evolution reaction electrocatalysis. J Power Sources 2019;438:226988.
[64] Anantharaj S, Kundu S. Do the evaluation parameters reflect intrinsic activity of electrocatalysts in electrochemical water splitting? ACS Energy Lett 2019;4:1260–4.
[65] Anantharaj S, Noda S. Appropriate use of electrochemical impedance spectroscopy in water splitting electrocatalysis. Chemelectrochem 2020;7:2297–308.
[66] Anantharaj S, Noda S. Dos and don'ts in screening water splitting electrocatalysts. Energy Adv 2022;1:511–23.
[67] Anantharaj S, Karthik PE, Noda S. The significance of properly reporting turnover frequency in electrocatalysis research. Angew Chem Int Ed 2021;60:23051–67.
[68] Yu X, Zhao Z, Pei C. Surface oxidized iron-nickel nanorods anchoring on graphene architectures for oxygen evolution reaction. Chin Chem Lett 2021;32:3579–83.